

# Cartesian Atomic Moment Machine Learning Interatomic Potentials

Mingjian Wen,<sup>\*</sup> Wei-Fan Huang, Jin Dai, and Santosh Adhikari

*Department of Chemical and Biomolecular Engineering,*

*University of Houston, Houston, TX, 77204, USA*

(Dated: November 20, 2024)

Machine learning interatomic potentials (MLIPs) have substantially advanced atomistic simulations in materials science and chemistry by providing a compelling balance between accuracy and computational efficiency. While leading MLIPs rely on representations of atomic environments using spherical tensors, Cartesian representations offer potential advantages in simplicity and efficiency. In this work, we introduce Cartesian Atomic Moment Potentials (CAMP), an approach equivalent to models based on spherical tensors but operating entirely in the Cartesian space. CAMP constructs atomic moment tensors from neighboring atoms and combines these through tensor products to incorporate higher body-order interactions, which can provide a complete description of local atomic environments. By integrating these into a graph neural network (GNN) framework, CAMP enables physically-motivated and systematically improvable potentials. It requires minimal hyperparameter tuning that simplifies the training process. The model demonstrates excellent performance across diverse systems, including periodic structures, small organic molecules, and two-dimensional materials. It achieves accuracy, efficiency, and stability in molecular dynamics simulations surpassing or comparable to current leading models. By combining the strengths of Cartesian representations with the expressiveness of GNNs, CAMP provides a powerful tool for atomistic simulations to accelerate materials understanding and discovery.

Machine learning interatomic potentials (MLIPs) have been widely employed in molecular simulations to investigate the properties of all kinds of materials, ranging from small organic molecules to inorganic crystals and biological systems. MLIPs offer a balance between accuracy and efficiency [1–4], making them a suitable choice standing between first-principles methods such as density functional theory (DFT) and classical interatomic potentials such as the embedded atom method (EAM) [5].

Since the introduction of the pioneering Behler–Parrinello neural network (BPNN) potential [6] and the Gaussian approximation potential (GAP) [7], many valuable MLIPs have been developed [8–19]. At the same time, techniques have emerged to assess the reliability of MLIP predictions by quantifying uncertainties and evaluating their influence on downstream properties [20–24]. Despite this progress, the pursuit of enhancing and developing new MLIPs remains ongoing. Current leading MLIPs in terms of accuracy and stability in molecular dynamics (MD) simulations are those based on graph neural networks (GNNs). These models represent an atomic structure as a graph and perform message passing between atoms to propagate information [25]. The passed messages can be either scalars [10, 12], vectors [13], or, more generally, tensors [16–19]. Using GNNs, a couple of universal MLIPs have recently been developed [26–32], which can cover a wide range of materials with chemical species across the periodic table.

At the core of any MLIP lies a description of the atomic environment, which converts the information contained in an atomic neighborhood to a numerical representation that can then be updated and used in an ML regres-

sion algorithm. The representation must satisfy certain symmetries (invariance to permutation of atoms, and invariance or equivariance to translation, rotation, and inversion) inherent to atomic systems. Despite the diverse choice of ML regression algorithms, the atomic environment representation is typically constructed by expanding atomic positions on some basis functions. Early works employ manually crafted basis functions for the bond distances and bond angles, such as the atom-centered symmetry functions used in BPNN [6] and ANI-1 [33]. More systematic representations have been developed and adopted in GAP [7], SNAP [34], ACE [35], NequIP [17], and MACE [16], among others. In these models, a representation is obtained by first expanding the atomic environment using a radial basis (e.g., Chebyshev polynomials) and the spherical harmonics angular basis to obtain tensorial equivariant features. The equivariant features are then updated and finally contracted to yield the scalar potential energy.

Another approach seeks to develop atomic representations and MLIPs entirely in Cartesian space, bypassing the need for spherical harmonics. This can potentially offer greater simplicity and reduced complexity compared to models using spherical representations. The MTP model by Shapeev [36] adopted this approach, which constructs Cartesian moment tensors to capture the angular information of an atomic environment. It has been shown that MTP and ACE are highly related given that a moment tensor can be expressed using spherical harmonics [37]. TeaNet [18] and TensorNet [19] have explored using Cartesian tensors limited to second rank to create MLIPs. The recent CACE model [38] has extended the atomic cluster expansion to Cartesian space and subsequently built MLIPs on this foundation. These works represent excellent efforts toward building MLIPs using

---

<sup>\*</sup> mjwen@uh.edu

a fully Cartesian representation of atomic environments. However, their performance has not yet matched that of models built using spherical tensors.

In this work, we propose Cartesian Atomic Moment Potential (CAMP), a systematically improvable MLIP developed in the Cartesian space under the GNN framework. Inspired by MTP [36], CAMP employs physically motivated moment tensors to characterize atomic environments. It then generates hyper moments through tensor products of these moment tensors, effectively capturing higher-order interactions. We have devised specific construction rules for atomic and hyper moment tensors that direct message flow from higher-rank to lower-rank tensors, ultimately to scalars. This approach aligns with our objective of modeling potential energy (a scalar quantity) and significantly reduces the number of moment tensors, enhancing computational efficiency. These moment tensors are subsequently integrated into a message-passing GNN framework, undergoing iterative updates and refinement to form the final CAMP. To evaluate the model’s performance, we have conducted tests across diverse material systems, including periodic LiPS inorganic crystals [17] and bulk water [39], non-periodic small organic molecules [8], and partially periodic two-dimensional (2D) graphene [40]. These comprehensive benchmarking studies demonstrate that CAMP is an accurate, efficient, and stable MLIP for molecular simulations.

## RESULTS

### A. Model Architecture

CAMP is a GNN model that processes atomic structures, utilizing atomic coordinates, atomic numbers, and cell vectors as input, and predicts the total potential energy, stresses on the structure, and the forces acting on individual atoms.

Fig. 1 presents a schematic overview of the model architecture. We discuss the key components and model design choices below.

#### Atomic graph

An atomic structure is represented as a graph  $G(V, E)$  consisting of a set of nodes  $V$  and a set of edges  $E$ . Each node in  $V$  represents an atom, and an edge in  $E$  is created between two atoms if they are within a cutoff distance of  $r_{\text{cut}}$  (Fig. 1a). An atom node  $i$  is described by a 3-tuple  $(\mathbf{r}^i, z^i, \mathbf{h}^i)$ , where  $\mathbf{r}^i$  is the position of the atom,  $z^i$  is the atomic number, and  $\mathbf{h}^i$  is the atom feature. The vector  $\mathbf{r}^{ij} = \mathbf{r}^j - \mathbf{r}^i$  associated with the edge from atom  $i$  to atom  $j$  gives their relative position.

The atom feature  $\mathbf{h}^i$  is a set of tensors that carry two indices  $u$  and  $v$ , becoming  $\mathbf{h}_{uv}^i$  in its full form, where  $u$

and  $v$  denote the *channel* and *rank* of each feature tensor, respectively. The use of channels allows for multiple copies of tensors of the same rank, helping to increase the expressiveness of the feature. The atom features are mixed across different channels using a linear mapping:

$$\mathbf{h}_{uv}^i = \sum_{u'} W_{uu'} \mathbf{h}_{u'v}^i, \quad (1)$$

where  $W_{uu'}$  are trainable parameters.

#### Radial basis

The edge length  $r^{ij} = \|\mathbf{r}^{ij}\|$  is expanded using a set of radial basis functions,  $B_u(r^{ij}, z^i, z^j)$ , indexed by the channel  $u$ . Following MTP [36, 41], each basis function is a linear combination of the Chebyshev polynomials of the first kind  $Q^\beta$ :

$$B_u(r^{ij}, z^i, z^j) = \sum_{\beta=0}^{N_\beta} W_{uz^i z^j}^\beta Q^\beta \left( \frac{r^{ij}}{r_{\text{cut}}} \right), \quad (2)$$

where  $N_\beta$  denotes the maximum degree of the Chebyshev polynomials. Separate trainable parameters  $W_{uz^i z^j}^\beta$  are used for different atom pairs, enabling customized radial basis dependent on their atomic numbers  $z^i$  and  $z^j$ . Moreover, the radial basis  $B_u$  allows the model to scale to any number of chemical species without increasing the model size.

#### Angular part

The angular information of an atomic environment is contained in the normalized edge vectors,  $\hat{\mathbf{r}} = \mathbf{r}/r$ , where we have omitted the atom indices  $i$  and  $j$  in  $\mathbf{r}^{ij}$  and  $r^{ij}$  for simplicity. Unlike many existing models that expand it on spherical harmonics, we directly adopt the Cartesian basis. We define the *generalized dyadic tensor* of rank  $v$  constructed from  $\hat{\mathbf{r}}$  as

$$\mathbf{D}_v = \hat{\mathbf{r}} \otimes \hat{\mathbf{r}} \otimes \cdots \otimes \hat{\mathbf{r}} \quad (v \text{ of } \hat{\mathbf{r}}), \quad (3)$$

where  $\otimes$  denotes a tensor product. For example,  $\mathbf{D}_0 = 1$  is a scalar,  $\mathbf{D}_1 = \hat{\mathbf{r}} = [\hat{r}_x, \hat{r}_y, \hat{r}_z]$  is a vector, and  $\mathbf{D}_2 = \hat{\mathbf{r}} \otimes \hat{\mathbf{r}}$  is a rank-2 tensor, which can be written in a matrix form as

$$\mathbf{D}_2 = \begin{bmatrix} \hat{r}_x^2 & \hat{r}_x \hat{r}_y & \hat{r}_x \hat{r}_z \\ \hat{r}_y \hat{r}_x & \hat{r}_y^2 & \hat{r}_y \hat{r}_z \\ \hat{r}_z \hat{r}_x & \hat{r}_z \hat{r}_y & \hat{r}_z^2 \end{bmatrix}, \quad (4)$$

where  $\hat{r}_x$ ,  $\hat{r}_y$ , and  $\hat{r}_z$  are the Cartesian components of  $\hat{\mathbf{r}}$  (Fig. 1b). Any  $\mathbf{D}_v$  is symmetric, as can be seen from the definition in Eq. (3). In CAMP, the angular information of an atomic environment is captured by  $\mathbf{D}_0$ ,  $\mathbf{D}_1$ ,  $\mathbf{D}_2$ , and so on, which are straightforward to evaluate. In full notation with atom indices, a generalized dyadic tensor is written as  $\mathbf{D}_v^{ij}$ .

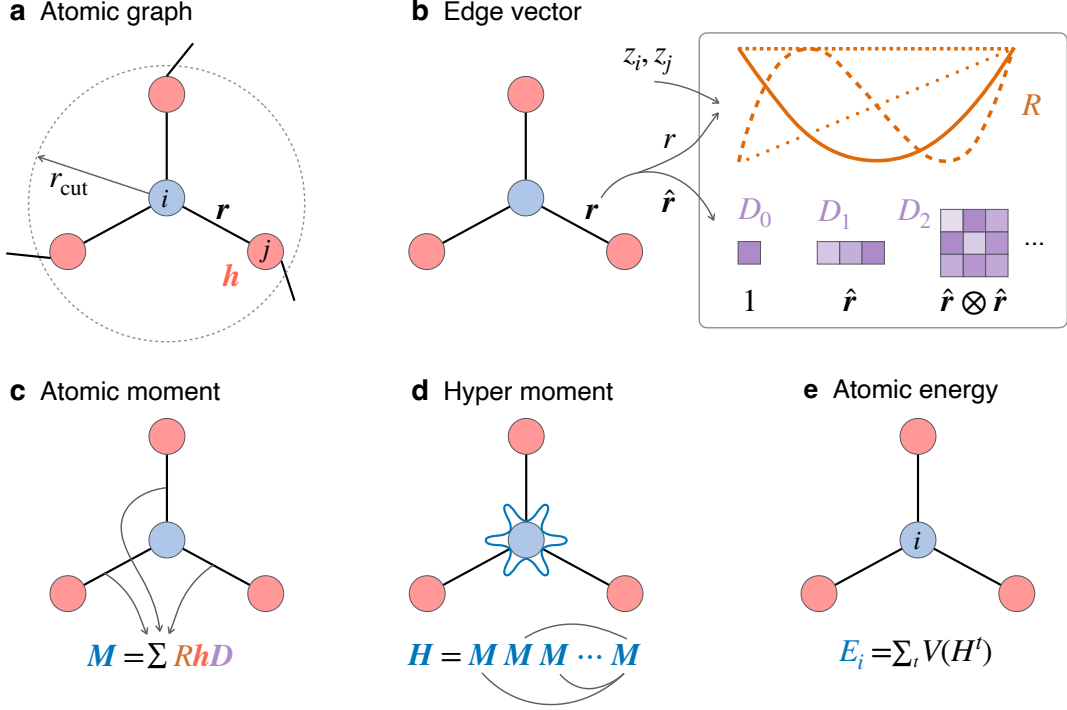


FIG. 1. **Schematic overview of the CAMP model architecture.** **a** An atomic structure is represented as a graph. Each atom is associated with a feature  $\mathbf{h}$ , and all atoms within a distance of  $r_{\text{cut}}$  to a center atom  $i$  constitute its local atomic neighborhood. **b** Atomic numbers  $z_i$  and  $z_j$  of a pair of atoms and their relative position vector  $\mathbf{r}$  are expanded into the radial part  $\mathbf{R}$  and angular part  $\mathbf{D}$ . **c** Atomic moment  $\mathbf{M}$  of the central atom is obtained by aggregating information from neighboring atoms. **d** Hyper moment  $\mathbf{H}$  of the central atom is computed by self-interactions between atomic moments. **e** Hyper moments  $\mathbf{H}^t$  of different layers  $t$  are used to construct the energy of the central atom via some mapping function  $V$ .

### Atomic moment

A representation of the local atomic environment of an atom is constructed from the radial basis, angular part, and atom feature, which we call the *atomic moment*:

$$\mathbf{M}_{uv,p}^i = \sum_{j \in \mathcal{N}_i} R_{uvv_1v_2} \mathbf{h}_{uv_1}^j \odot^c \mathbf{D}_{v_2}^{ij}, \quad (5)$$

where  $\mathcal{N}_i$  denotes the set of neighboring atoms within a distance of  $r_{\text{cut}}$  to atom  $i$ . The radial part is obtained by passing the radial basis through a multi-layer perceptron (MLP),  $R_{uvv_1v_2} = \text{MLP}(B_u)$ . For different combinations of  $u$ ,  $v$ ,  $v_1$ , and  $v_2$ , different MLPs are used. The symbol  $\odot^c$  denotes a degree- $c$  contraction between two tensors. For example, for tensor  $\mathbf{A}$  and  $\mathbf{B}$  of rank-2 and rank-3, respectively,  $\mathbf{A} \odot^2 \mathbf{B}$  means  $C_k = \sum_{ij} A_{ij} B_{ijk}$ , resulting in a rank-1 tensor. In other words,  $c$  is the number of indices contracted away in each of the two tensors involved in the contraction; thus, the output tensor has a rank of  $v = v_1 + v_2 - 2c$ . We denote the combination of  $v_1$ ,  $v_2$ , and  $c$  as a *path*:  $p = (v_1, v_2, c)$ . In Eq. (5), multiple paths can result in output tensors of the same rank  $v$ . For example,  $p = (2, 3, 2)$  and  $p = (1, 2, 1)$  both lead to atomic moment rank  $v = 1$ . This is why the index  $p$  is used in  $\mathbf{M}_{uv,p}^i$  to denote from which path the atomic moment is obtained.

The atomic moment carries significant physical implications. For a physical quantity  $Q$  at a distance  $r$  from a reference point, the  $n$ th moment of  $Q$  is defined as  $r^n Q$ . For example, when  $Q$  represents a force and  $n = 1$ ,  $rQ$  corresponds to the torque. Eq. (5) generalizes this concept, with the feature  $\mathbf{h}_{uv_1}^j$  of atom  $j$  acting as  $Q$ , and  $\mathbf{D}_{v_2}^{ij}$  serving as the “distance”  $r$ . The radial part  $R_{uvv_1v_2}$  functions as a weighting factor, modulating the relative contribution of different atoms  $j$ . This is why we refer to the output in Eq. (5) as the atomic moment.

By construction, the atomic moment is symmetric. This is because, first, both  $\mathbf{h}_{uv_1}^j$  (explained below around Eq. (9)) and  $\mathbf{D}_{v_2}^{ij}$  are symmetric; second, an additional constraint  $c = v_1 < v_2$  is imposed. The constraint means that the indices of  $\mathbf{h}_{uv_1}^j$  are thus the output atomic moment has  $v = v_2 - v_1$  indices from  $\mathbf{D}_{v_2}^{ij}$ . A detailed example of evaluating Eq. (5) is provided in the Supplementary Information (SI).

Atomic moment tensors of the same rank  $v$  from different paths are combined using a linear layer:

$$\mathbf{M}_{uv} = \sum_p W_{uv,p} \mathbf{M}_{uv,p}, \quad (6)$$

in which  $W_{uv,p}$  are trainable parameters and the atom index  $i$  is omitted for simplicity.

From atomic moments, we create the *hyper moment* as

$$\mathbf{H}_{uv,p} = \mathbf{M}_{uv_1} \odot^{c_1} \mathbf{M}_{uv_2} \odot^{c_2} \dots \odot^{c_{n-1}} \mathbf{M}_{uv_n}. \quad (7)$$

Atomic moments capture two-body interactions between a center atom and its neighbors. Three-body, four-body, and higher-body interactions are incorporated into the hyper moments via the self-interactions between atomic moments in Eq. (7). The hyper moments can provide a complete span of the local atomic environment by increasing the interaction order [36, 37], which is crucial for constructing systematically improbable MLIPs. The hyper moments are analogous to the B-basis used in ACE [35] and MACE [16].

The primary target of an MLIP model is the potential energy, a scalar quantity. Aligned with this, we construct hyper moments such that information flows from higher-rank atomic moment tensors to lower-rank ones, ultimately to scalars. Specifically, we impose the following rule: let  $\mathbf{M}_{uv_n}$  be the tensor of the highest rank among all atomic moment tensors in Eq. (7), then possible contractions are only between it and the other atomic moments, but not between  $\mathbf{M}_{uv_1}$  and  $\mathbf{M}_{uv_2}$ , and so forth. This design choice substantially reduces the number of hyper moments, which simplifies both the model architecture and the overall training process. Moreover, similar to the atomic moment, the indices of lower-rank atomic tensors  $\mathbf{M}_{uv_1}, \mathbf{M}_{uv_2}, \dots$  are completely contracted away, and therefore we have  $v = v_n - (v_1 + v_2 + \dots + v_{n-1})$ . This guarantees that  $\mathbf{H}_{uv,p}$  is constructed to be symmetric. Multiple contractions can result in hyper moments of the same rank  $v$ ; they are indexed by  $p$ . A detailed example of evaluating Eq. (7) to create hyper moments is provided in the SI.

### Message Passing

The messages to an atom  $i$  from all neighboring atoms are chosen to be a linear expansion over the hyper moments:

$$\mathbf{m}_{uv} = \sum_p W_{uv,p} \mathbf{H}_{uv,p}. \quad (8)$$

Atom features are then updated using a residual connection [42] by linearly combining the message and the atom feature of the previous layer:

$$\mathbf{h}_{uv}^t = \sum_{u'} W_{1,uu'} \mathbf{m}_{u'v} + \sum_{u'} W_{2,uu'} \mathbf{h}_{u'v}^{t-1}, \quad (9)$$

where  $t$  is the layer index. Atom features in the input layer  $\mathbf{h}_{uv}^0$  only consist of scalars  $h_{u0}^0$ , obtained as a  $u$ -dimensional embedding of the atomic number  $z$ . By construction,  $\mathbf{h}_{uv}^t$  is symmetric.

The message passing is performed multiple times  $T$ . We find that typical values of two or three are good enough based on benchmarking studies to be discussed in the following sections. The atomic energy of atom  $i$  is then obtained from the scalar atom features  $h_{u0}^{i,t}$  from all layers:

$$E^i = \sum_{t=1}^T V(\mathbf{h}_{u0}^{i,t}). \quad (10)$$

$V$  is set to an MLP for the last layer  $T$ , and a linear function for others layers, that is  $V(\mathbf{h}_{u0}^{i,t}) = \sum_u W_u^t \mathbf{h}_{u0}^{i,t}$  for  $t < T$ . Atomic energies of all atoms are summed to get the total potential energy

$$E = \sum_i E^i. \quad (11)$$

Forces on atom  $i$  can then be computed as

$$\mathbf{F}_i = -\frac{\partial E}{\partial \mathbf{r}_i}. \quad (12)$$

### Computational complexity

The most computationally demanding part of CAMP is creating the atomic moments and hyper moments. Although the need to generate atomic and hyper moments adds to the computational cost, it is still more efficient compared to methods based on spherical tensors such as NequIP [17] and MACE [16]. To illustrate, let  $v_{\max}$  represent the maximum rank of tensors used in the model. This implies that all features  $\mathbf{h}$ , atomic moments  $\mathbf{M}$ , and hyper moments  $\mathbf{H}$  have ranks up to  $v_{\max}$ . The time complexity for constructing both the atomic moment in Eq. (5) and the hyper moment in Eq. (7) is  $\mathcal{O}(3^{v_{\max}})$  (with detailed analysis in the SI). In contrast, for spherical tensor-based models such as NequIP [17] and MACE [16], the time complexity of the Clebsch–Gordan tensor product is  $\mathcal{O}(L^6)$ , where  $L$ , analogous to  $v_{\max}$  in Cartesian tensors, is the maximum rank of the irreducible spherical tensors. Empirical evidence suggests that for many material systems, using  $L$  values around three yields models with good accuracy. In such cases, Cartesian tensor-based models like CAMP prove to be more computationally efficient.

### B. Inorganic crystals

We first test CAMP on a dataset of inorganic lithium phosphorus sulfide (LiPS) solid-state electrolytes [17]. Multiple models were trained using varying numbers of training samples (10, 100, 1000, and 2500), validated on

TABLE 1. **Performance of CAMP on the LiPS dataset.** MAEs of energy and forces are in the units of meV/atom and meV/Å, respectively.

| Training size |        | NequIP      | CAMP        |
|---------------|--------|-------------|-------------|
| 10            | Energy | 2.03        | <b>1.62</b> |
|               | Forces | 97.8        | <b>72.7</b> |
| 100           | Energy | 0.44        | <b>0.43</b> |
|               | Forces | 25.8        | <b>22.5</b> |
| 1000          | Energy | <b>0.12</b> | <b>0.12</b> |
|               | Forces | 7.7         | <b>7.4</b>  |
| 2500          | Energy | <b>0.08</b> | <b>0.08</b> |
|               | Forces | <b>4.7</b>  | 4.9         |

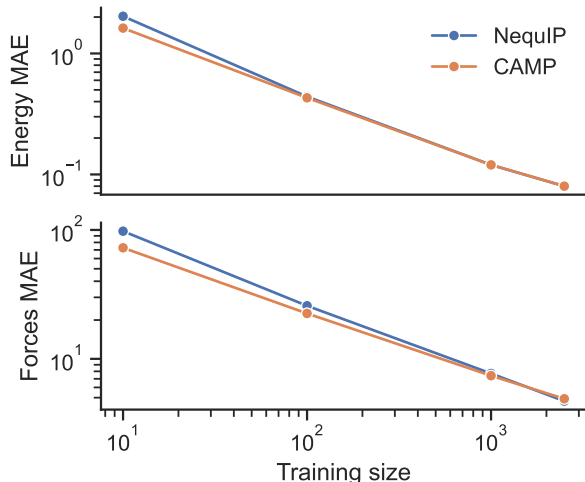


FIG. 2. **Learning curve of CAMP.** On a log-log scale, the MAEs of both energy (meV/atom) and forces (meV/Å) decrease linearly with the training set size.

1000 samples, and tested on 5000 samples (training details in Methods). Mean absolute errors (MAEs) of energy and forces on the test set are listed in Table 1. Compared with NequIP [17], CAMP yields smaller or equal errors on seven of the eight tasks. The learning curve in Fig. 2 exhibits a linear decrease in both energy and forces MAEs on a log-log scale as the number of training samples increases. These results demonstrate CAMP’s accuracy and its capacity for further improvement with increased data.

We further examine the performance in MD simulations, focusing on computing the diffusivity of lithium ions ( $\text{Li}^+$ ) in LiPS. Diffusivity is a crucial characteristic for assessing the potential of solid materials as electrolytes in next-generation solid-state batteries. Following existing benchmarking studies [43], we trained another model with 19000 structures with the same validation and test sets discussed above. Five structures were randomly selected from the test set and an independent MD simulation was performed for each structure. As seen in Fig. 3, CAMP accurately captures the structural information of LiPS, reproducing the radial distribution function (RDF) and angular distribution function (ADF)

of the S–P–S tetrahedral angle (Fig. S1 in the SI) from ab initio molecular dynamics (AIMD) simulations.

CAMP can yield stable MD simulations. It is known that MLIPs that perform well on energy and forces do not necessarily guarantee high-quality MD simulations. In particular, MD simulations can collapse due to model instability. Therefore, before calculating the diffusivity, we checked the simulation stability. The stability is measured as the difference between the RDF averaged over a time window and the RDF of the entire simulation (see Methods). CAMP shows excellent stability, reaching the entire simulation time of 50 ps in all five simulations (Table 2). In Ref. [43], a small timestep of 0.25 fs was adopted in the MD simulations using the models in Table 2. We also tested CAMP with a large timestep of 1 fs and found that all five simulations are still stable up to 50 ps (see Fig. S2 in the SI).

The diffusion coefficient  $D$  of  $\text{Li}^+$  in LiPS calculated from CAMP is in good agreement with the AIMD result. After confirming the stability,  $D$  was calculated using the Einstein equation by fitting a linear line between the mean squared displacement (MSD) of  $\text{Li}^+$  and the correlation time (see Methods). The MSDs of the five MD runs are shown in Fig. 3c, from which the diffusion coefficient is calculated as  $D = (1.08 \pm 0.08) \times 10^{-5} \text{ cm}^2/\text{s}$ . This agrees reasonably well with AIMD result of  $1.37 \times 10^{-5} \text{ cm}^2/\text{s}$  [17].

### C. Bulk water

To evaluate CAMP’s ability to model complex liquid systems, we test it on a dataset of bulk water [39]. See Methods Dataset and training details are in Root-mean-square errors (RMSEs) of energy and forces on the test set are listed in Table 3. In general, GNN models (RE-ANN [50], NequIP [17], MACE [16], and CACE [38]) have smaller errors than single layer ACE [35] and descriptors-based BPNN [39]. Our CAMP achieves the best performance on both energy and forces, with RMSEs of 0.59 meV/atom and 34 meV/Å, respectively. We observe that CACE [38] demonstrates comparable RMSEs on energy when compared to CAMP. Similar to CAMP, CACE [38] is a recent model developed entirely in Cartesian space; however, the physical motivations and model architectures of CAMP and CACE differ. We believe these architectural differences contribute to CAMP’s improved RMSEs on forces relative to CACE [38]. The connections of CAMP with other models are further elaborated in Discussion.

CAMP accurately reproduces experimental structural and dynamical properties of water. Fig. 4 shows the oxygen–oxygen RDF of water from MD simulations using CAMP (computation details in Methods), together with experimental observations obtained from neutron diffraction [48] and x-ray diffraction [49]. The RDF by CAMP nearly overlaps with the x-ray diffraction result, demonstrating its ability to capture the delicate structural fea-

TABLE 2. **Results on LiPS for models developed with 19000 training samples.** MAE of forces and MAE of  $\text{Li}^+$  diffusivity are reported in  $\text{meV}/\text{\AA}$  and  $10^{-5} \text{cm}^2/\text{s}$ , respectively. The reference diffusivity is  $1.35 \times 10^{-5} \text{cm}^2/\text{s}$ . Stability is measured by MD simulation time in picoseconds, with standard deviations obtained from 5 independent runs shown in parentheses. All results are obtained from Ref. [43], except those for CAMP.

|             | DeepPot-SE [44]  | SchNet [10]       | DimeNet [12]      | PaiNN [13]        | SphereNet [45]    | ForceNet [46]     | GemNet-T [47]     | NequIP [17]       | CAMP              |
|-------------|------------------|-------------------|-------------------|-------------------|-------------------|-------------------|-------------------|-------------------|-------------------|
| Forces      | 40.5             | 28.8              | 3.2               | 11.7              | 8.3               | 12.8              | 1.3               | 3.7               | 3.6               |
| Diffusivity |                  | 0.38              | 0.30              | 0.40              | 0.40              |                   | 0.24              | 0.34              | 0.18              |
| Stability   | 4 <sub>(3)</sub> | 50 <sub>(0)</sub> | 48 <sub>(4)</sub> | 50 <sub>(0)</sub> | 50 <sub>(0)</sub> | 26 <sub>(8)</sub> | 50 <sub>(0)</sub> | 50 <sub>(0)</sub> | 50 <sub>(0)</sub> |

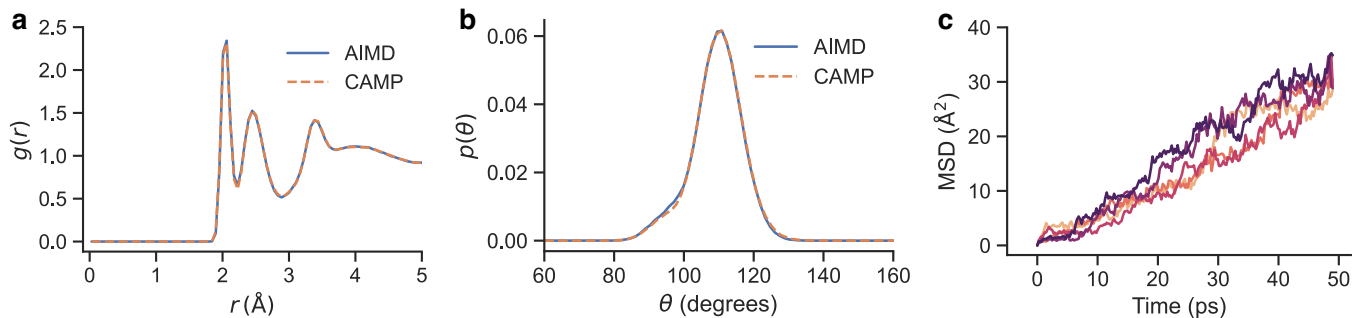


FIG. 3. **MD simulation results on LiPS.** **a** Radial distribution function. **b** Angular distribution function for the S–P–S tetrahedral angle. **c** Mean squared displacement of  $\text{Li}^+$  in LiPS. Five MD simulations are performed, and the average  $\text{Li}^+$  diffusion coefficient is  $D = 1.08 \times 10^{-5} \text{cm}^2/\text{s}$ .

TABLE 3. **Model performance on the water dataset.** RMSEs of energy and forces are in the units of  $\text{meV}/\text{atom}$  and  $\text{meV}/\text{\AA}$ , respectively. Speed is measured as completed steps per second in MD simulations of the water system of 192 atoms, using a single NVIDIA V100 GPU. All energy and forces RMSE results, except CAMP, are from Ref. [38]. DeePMD and NequIP running speed results are from Ref. [43].

|        | BPNN [39] | ACE [35] | REANN [50] | DeePMD [9] | NequIP [17] | MACE [16] | CACE [38]   | CAMP        |
|--------|-----------|----------|------------|------------|-------------|-----------|-------------|-------------|
| Energy | 2.3       | 1.7      | 0.8        | 2.1        | 0.94        | 0.63      | <b>0.59</b> | <b>0.59</b> |
| Forces | 120       | 99       | 53         | 92         | 45          | 36        | 47          | <b>34</b>   |
| Speed  |           |          |            | 61.8       | 3.9         |           | 9.8         | 14.2        |

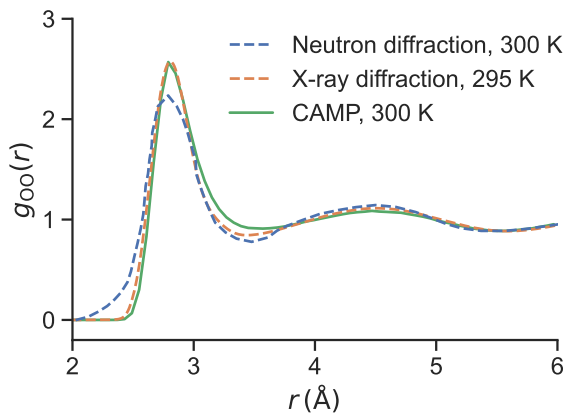


FIG. 4. **Oxygen–Oxygen RDF of water.** Experimental neutron diffraction [48] and x-ray diffraction [49] results are shown for comparison.

tures of water. We also calculated the diffusion coefficient of water ( $1 \text{g}/\text{cm}^3$ ) at 300 K to be  $D = 2.76 \times 10^{-5} \text{cm}^2/\text{s}$ , which is in excellent agreement with AIMD results of

$2.67 \times 10^{-5} \text{cm}^2/\text{s}$  [51]. The model shows superior stability for water, producing stable MD simulations at high temperatures up to 1500 K. The RDF and diffusion coefficient at various high temperatures are presented in Fig. S3 in the SI.

We examine the efficiency of CAMP by measuring the number of completed steps per second in MD simulations. It is not a surprise that DeePMD [9] runs much faster thanks to its simplicity in the model architecture, although its accuracy falls short when compared with more recent models (Table 3). For those more accurate models, CAMP is about 1.4 and 3.6 times faster than CACE [38] and NequIP [17], respectively, on the water system of 192 atoms. More running speed data of other models are provided in Table S1 in the SI.

#### D. Small organic molecules

The MD17 dataset consists of AIMD trajectories of several small organic molecules [8]. For each molecule, we trained CAMP on 950 random samples, validated on 50 samples, and the rest were used for testing (dataset

TABLE 4. **Model performance on the MD17 dataset.** MAEs of energy and forces are in the units of meV and meV/Å, respectively. **Bold:** smallest; underline: second smallest.

| Molecule       |        | SchNet [10] | DimeNet [52] | sGDML [8] | PaiNN [13]  | NewtonNet [53] | NequIP [17] | CAMP        |
|----------------|--------|-------------|--------------|-----------|-------------|----------------|-------------|-------------|
| Aspirin        | Energy | 16.0        | 8.8          | 8.2       | <u>6.9</u>  | 7.3            | <b>5.7</b>  | 7.9         |
|                | Forces | 58.5        | 21.6         | 29.5      | <u>14.7</u> | 15.1           | <b>8.0</b>  | 19.0        |
| Ethanol        | Energy | 3.5         | 2.8          | 3.0       | 2.7         | 2.6            | <b>2.2</b>  | <u>2.5</u>  |
|                | Forces | 16.9        | 10.0         | 14.3      | 9.7         | 9.1            | <b>3.1</b>  | <u>7.6</u>  |
| Malonaldehyde  | Energy | 5.6         | 4.5          | 4.3       | <u>3.9</u>  | 4.2            | <b>3.3</b>  | <u>3.9</u>  |
|                | Forces | 28.6        | 16.6         | 17.8      | <u>13.8</u> | 14.0           | <b>5.6</b>  | <u>12.9</u> |
| Naphthalene    | Energy | 6.9         | 5.3          | 5.2       | 5.0         | 5.1            | <u>4.9</u>  | <b>4.2</b>  |
|                | Forces | 25.2        | 9.3          | 4.8       | <u>3.3</u>  | 3.6            | <b>1.7</b>  | 3.7         |
| Salicylic acid | Energy | 8.7         | 5.8          | 5.2       | <u>4.9</u>  | 5.0            | <b>4.6</b>  | <b>4.6</b>  |
|                | Forces | 36.9        | 16.2         | 12.1      | <u>8.5</u>  | <u>8.5</u>     | <b>3.9</b>  | 11.0        |
| Toluene        | Energy | 5.2         | 4.4          | 4.3       | <u>4.1</u>  | <u>4.1</u>     | <b>4.0</b>  | 4.5         |
|                | Forces | 24.7        | 9.4          | 6.1       | 4.1         | <u>3.8</u>     | <b>2.0</b>  | <u>3.8</u>  |
| Uracil         | Energy | 6.1         | 5.0          | 4.8       | 4.5         | <u>4.6</u>     | <u>4.5</u>  | <b>4.4</b>  |
|                | Forces | 24.3        | 13.1         | 10.4      | <u>6.0</u>  | 6.5            | <b>3.3</b>  | 7.5         |

and training details in Methods). MAEs of energy and forces by CAMP and other MLIPs are listed in Table 4. While NequIP [17] generally maintains high performance, CAMP demonstrates high competitiveness. It surpasses NequIP in energy predictions for three out of seven molecules and ranks second in both energy and force predictions across various cases.

We further tested the ability of CAMP to maintain long-time stable MD simulations. Following the benchmarking study in Ref. [43], 9500, 500, and 10000 molecules were randomly sampled for training, validation, and testing, respectively. With the trained models, we performed MD simulations at 500 K for 300 ps and examined the stability by measuring the bond length change during the simulations (see Methods). Fig. 5 presents the results for Aspirin and Ethanol (numerical values in Table S2 in the SI). In general, a small forces MAE does not guarantee stable MD simulations [43], as seen from a comparison between ForceNet and GemNet-T. GemNet-T has a much smaller MAE of forces, but its stability is not as good as ForceNet. For CAMP, its MAE of forces is slightly larger than that of, e.g. GemNet-T and SphereNet, but it can maintain stable MD simulations for the entire simulation time of 300 ps, a significant improvement over most of the existing models.

In terms of running speed, similar patterns are observed here as those reported in the water system. Models based on simple scalar features such as SchNet [10] and DeepPot-SE [44] are faster than those based on tensorial features, although they are far less accurate (Fig. 5). For both Aspirin and Ethanol, CAMP can complete about 33 steps per second in MD simulations on a single NVIDIA V100 GPU, which is approximately 1.2, 1.4, and 3.9 times faster than GemNet-T [47], SphereNet [45], and NequIP [17], respectively.

## E. Two-dimensional materials

In addition to periodic systems and small organic molecules, we evaluate the performance of CAMP on partially periodic 2D materials. These materials exhibit distinct physical and chemical properties. Despite their significance, to the best of our knowledge, no standardized benchmarking dataset exists for MLIPs specifically designed for 2D materials. We have thus constructed a new DFT dataset of bilayer graphene, building upon our previous investigations of carbon systems [40]. See Methods for detailed information on this new dataset.

Widely used empirical potentials for carbon systems, such as AIREBO [54], AIREBO-M [55], and LCBOP [56] have large errors in predicting both the energy and forces of bilayer graphene. The MAEs on the test set against DFT results are on the order of hundreds of meV/atom for energy and meV/Å for forces (Table 5). MLIPs such as hNN [40] (a hybrid model that combines BPNN [6] and Lennard-Jones [57]) can significantly reduce the errors; CAMP can further drive the MAEs down to 0.3 meV/atom for energy and 6.3 meV/Å for forces.

It is interesting to investigate the interlayer interaction between the graphene layers, which controls many structural, mechanical, and electronic properties of 2D materials [58, 59]. Here, we focus on the energetics in different stacking configurations: AB, AA, and saddle point (SP) stackings (Fig. 6a). Empirical models such as LCBOP cannot distinguish between the different stacking states at all. The interlayer energy versus layer distance curves are almost identical between AB and AA (Fig. 6b), and the generalized stacking fault energy surface is nearly flat (not shown), with a maximum value on the order of 0.01 meV/atom. This is also the case for AIREBO and AIREBO-M (we refer to Ref. [40] for plots). On the contrary, CAMP and hNN can clearly distinguish between the stackings. Both the interlayer energy versus layer distance curves and the generalized stacking fault energy surface agree well with DFT references,



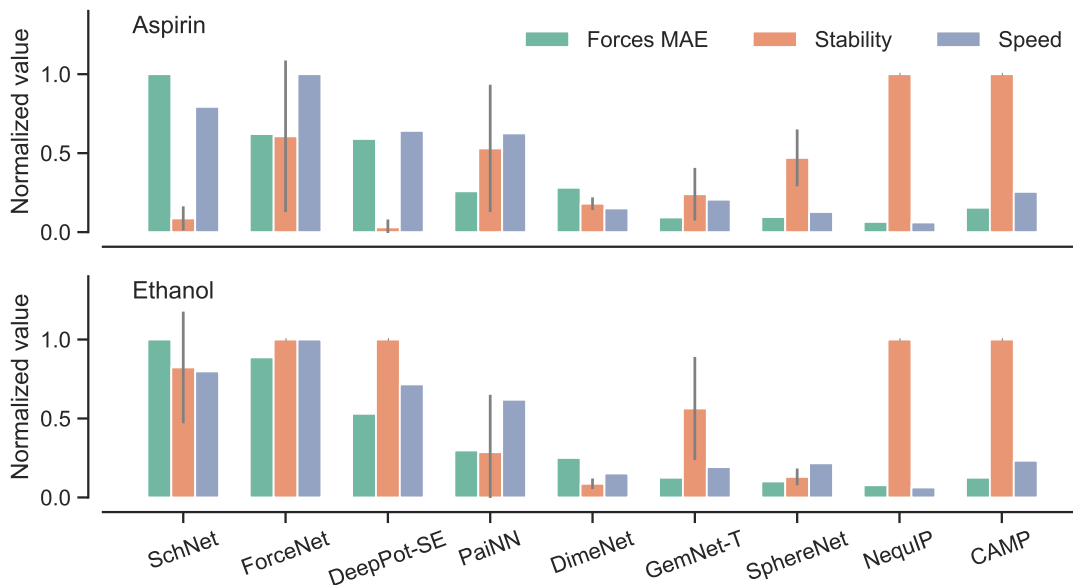


FIG. 5. **Comparison of MAE of forces, MD stability, and running speed on small molecules.** The forces MAE, stability, and running speed are normalized by their maximum values for easier visualization. All numerical values are provided in Table S2 in the SI. Error bars indicate the standard deviation from five MD runs using different starting atomic positions. Computational speed is measured on a single NVIDIA V100 GPU.

TABLE 5. **Results on the bilayer graphene dataset.** MAEs of the energy and forces are in the units of meV/atom and meV/Å, respectively.

|        | AIREBO [54] | AIREBO-M [55] | LCBOP [56] | hNN [40] | CAMP |
|--------|-------------|---------------|------------|----------|------|
| Energy | 659.9       | 671.2         | 718.3      | 1.4      | 0.3  |
| Forces | 194.6       | 186.9         | 166.1      | 46.0     | 6.3  |

and CAMP has a slightly better prediction of the energy barrier ( $\Delta E_{\text{SP-AB}}$ ) and the overall energy corrugation ( $\Delta E_{\text{AA-AB}}$ ). The hNN model is specifically designed as an MLIP for 2D materials, and its training process is complex, requiring separate training of the Lennard-Jones and BPNN components. In contrast, CAMP does not require such special treatment and is straightforward to train.

## DISCUSSION

In this work, we develop CAMP, a new class of MLIP that is based on atomic moment tensors and operates entirely in the Cartesian space. CAMP is designed to be physically inspired, flexible, and expressive, and it can be applied to a wide range of systems, including periodic structures, small organic molecules, and 2D materials. Benchmarking tests on these systems demonstrate that CAMP achieves performance surpassing or comparable to current leading models based on spherical tensors in terms of accuracy, efficiency, and stability. It is robust and straightforward to train, without the need to tune a large number of hyperparameters. In all the tested systems, we only need to set four hyperparameters: the

number of channels  $u$ , maximum tensor rank  $v_{\text{max}}$ , number of layers  $T$ , and cutoff radius  $r_c$  to achieve good performance.

CAMP is related to existing models in several ways. As shown in Ref. [37], ACE [35] and MTP [36] can be viewed as the same model, with the former constructed in the spherical space while the latter in the Cartesian space. Both are single-layer models without feature updates. Loosely speaking, MACE [16] and CAMP can be regarded as a generalization of the spherical ACE and Cartesian MTP, respectively, to multilayer GNNs with iterative feature updates and refinement. The atomic moment in Eq. (5) and hyper moment in Eq. (7) are related to the A-basis and B-basis in ACE and MACE. Moreover, CAMP generalizes existing Cartesian tensor models such as TeaNet [18] and TensorNet [19] that use at most second-rank tensors to arbitrary-rank tensors. Despite these connections, CAMP is unique in its design of the atomic moment and hyper moment, and the selection rules that govern the tensor contractions. These characteristics make CAMP a physically inspired, flexible, and expressive model.

Beyond energy and forces, CAMP can be extended to model tensorial properties. The atom features used in CAMP are symmetric Cartesian tensors, which can be



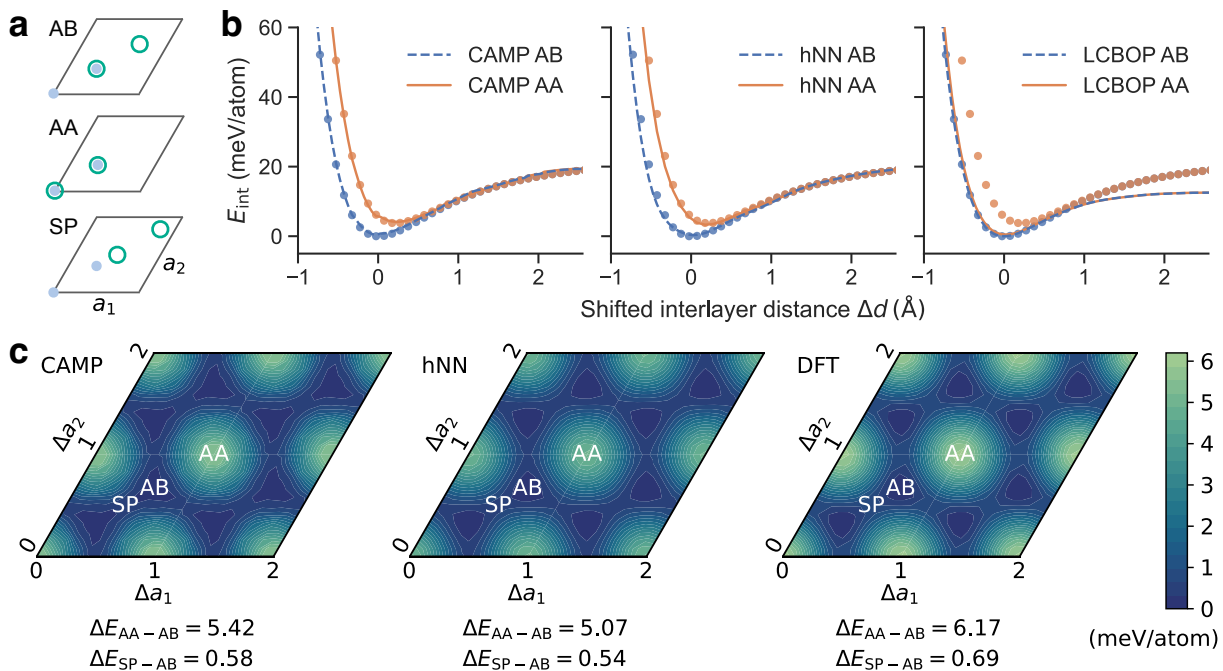


FIG. 6. **Interlayer energetics of bilayer graphene.** **a** Bilayer graphene in AB, AA, and saddle point (SP) stacking, where the blue solid dots represent atoms in the bottom layer, and the green hollow dots represent atoms in the top layer. **b** Interlayer energy  $E_{\text{int}}$  versus layer distance  $d$  of bilayer graphene in AB and AA stacking. The dots represent DFT results. The layer distance is shifted such that  $\Delta d = d - d_0$ , where  $d_0 = 3.4 \text{ \AA}$  is the equilibrium layer distance. **c** Generalized stacking fault energy of bilayer graphene. This is obtained by sliding the top layer against the bottom layer at a fixed layer distance of  $d_0$ , where  $\Delta a_1$  and  $\Delta a_2$  indicate the shifts of the top layer against the bottom layer, along the lattice vectors  $a_1$  and  $a_2$ , respectively.

used to output tensorial properties with slight modifications to the output block. For example, NMR tensors can be modeled by selecting and summing the scalar, vector, and symmetric rank-2 tensor components of the hyper moments, rather than using only the scalar component for potential energies. However, the current implementation of CAMP in PyTorch has certain limitations. All feature tensors are stored in full form, without exploiting the fact that they are symmetric. In addition, it is possible to extend CAMP to use irreducible representations of Cartesian tensors (basically symmetric traceless tensors), analogous to spherical irreducible representations used in spherical tensor models. Leveraging these symmetries and irreducible representations could further enhance model accuracy and improve time and memory efficiency. These are directions for future work.

## METHODS

**Dataset.** The LiPS dataset [17] consists of 250001 structures of lithium phosphorus sulfide ( $\text{Li}_{6.75}\text{P}_3\text{S}_{11}$ ) obtained from an AIMD trajectory. Each structure has 83 atoms, with 27 Li, 12 P, and 44 S. The data are randomized before splitting into training, validation, and test sets. The water dataset [39] consists of 1593 water structures, each with 192 atoms, generated with AIMD simulations at 300 K. The data are randomly split into train-

ing, validation, and test sets with a ratio of 90:5:5. The MD17 dataset [8] consists of AIMD trajectories of several small organic molecules. The number of data points for each molecule ranges from 133000 to 993000. Our new bilayer graphene dataset is derived from Ref. [40], with 6178 bilayer graphene configurations from stressed structures, atomic perturbations, and AIMD trajectories. The data were generated using DFT calculations with the PBE functional [60], and the many-body dispersion correction method [61] was used to account for van der Waals interactions. The data are split into training, validation, and test sets with a ratio of 8:1:1.

**Model training.** The models are trained by minimizing a loss function of energy and forces. For an atomic configuration  $\mathcal{C}$ , the loss is

$$l(\theta; \mathcal{C}) = w_E \left( \frac{E - \hat{E}}{N} \right)^2 + w_F \frac{\sum_{i=1}^N \|\mathbf{F}_i - \hat{\mathbf{F}}_i\|^2}{3N}, \quad (13)$$

where  $N$  is the number of atoms,  $E$  and  $\hat{E}$  are the predicted and reference energies, respectively, and  $\mathbf{F}_i$  and  $\hat{\mathbf{F}}_i$  are the predicted and reference forces on atom  $i$ , respectively. Both the energy weight  $w_E$  and force weight  $w_F$  are set to 1. The total loss to minimize at each optimization step is the sum of the losses of multiple configura-

tions,

$$L(\theta) = \sum_{j=1}^B l(\theta; \mathcal{C}_j), \quad (14)$$

where  $B$  is the mini-batch size.

The CAMP model is implemented in PyTorch [62] and trained with PyTorch Lightning [63]. We trained all models using the Adam optimizer [64] with an initial learning rate of 0.01, which is reduced by a factor of 0.8 if the validation error does not decrease for 100 epochs. The training batch size and allowed maximum number of training epochs vary for different datasets. Training is stopped if the validation error does not reduce for a certain number of epochs (see Table S3 in the SI). We use an exponential moving average with a weight 0.999 to evaluate the validation set as well as for the final model.

Regarding model structure, Chebyshev polynomials of degrees up to  $N_\beta = 8$  are used for the radial basis functions. Other hyperparameters include the number of channels  $u$ , maximum tensor rank  $v_{\max}$ , number of layers  $T$ , and cutoff distance  $r_{\text{cut}}$ . Optimal values of these hyperparameters are searched for each dataset, and typical values are around  $u = 32$ ,  $v_{\max} = 3$ ,  $T = 3$ , and  $r_{\text{cut}} = 5 \text{ \AA}$ . These result in small, parameter-efficient models with fewer than 125k parameters. Detailed hyperparameters for each dataset are provided in Table S4 in the SI.

**Diffusivity.** The diffusivity can be computed from MD simulations via the Einstein equation, which relates the MSD of particles to their diffusion coefficient:

$$D = \lim_{t \rightarrow \infty} \frac{\left\langle \frac{1}{N} \sum_i^N |\mathbf{r}_i(t) - \mathbf{r}_i(0)|^2 \right\rangle}{2nt}, \quad (15)$$

where the MSD is computed as the ensemble average (denoted by  $\langle \cdot \rangle$ ) using diffusing atoms,  $\mathbf{r}_i(t)$  represents the position of atom  $i$  at time  $t$ ,  $N$  is the total number of considered diffusion atoms,  $n$  denotes the number of dimensions (three here), and  $D$  is the diffusion coefficient. To solve for the diffusion coefficient  $D$ , we employ a linear fitting approach as implemented in ASE [65], where  $D$  is obtained as the slope of the MSD versus  $2nt$ .

The diffusivity of  $\text{Li}^+$  in LiPS was computed from MD simulations under the canonical ensemble using the Nosé–Hoover thermostat. Simulations were performed at a temperature of 520 K for a total of 50 ps, with a timestep of 0.25 fs, consistent with the settings reported in the benchmarking study in Ref. [43]. We similarly computed the diffusivity of water, but the simulations were performed at 300 K for 300 ps, with a timestep of 1 fs.

**Stability criteria.** For periodic systems, stability is monitored from the RDF  $g(r)$  such that a simulation becoming “unstable” at time  $t$  when [43]

$$\int_0^\infty \|\langle g(r) \rangle_t^{t+\tau} - \langle g(r) \rangle\| dr > \Delta, \quad (16)$$

where  $\langle \cdot \rangle$  denotes the average using the entire trajectory,  $\langle \cdot \rangle_t^{t+\tau}$  denotes the average in a time window  $[t, t+\tau]$ , and  $\Delta$  is a threshold. In other words, when the difference of the area under the RDF obtained from the time window and the entire trajectory exceeds  $\Delta$ , the simulation is considered unstable.

This criterion cannot be applied to characterize the stability of MD simulations where large structural changes are expected, such as in phase transitions or chemical reactions. However, for the LiPS system studied here, no such events are expected, and the RDF-based stability criterion is appropriate. We adopted  $\tau = 1 \text{ ps}$  and  $\Delta = 1$ , as proposed in Ref. [43].

For molecular systems, the stability is monitored through the bond lengths, and a simulation is considered “unstable” at time  $T$  when [43]

$$\max_{(i,j) \in \mathcal{B}} |r^{ij}(T) - b^{ij}| > \Delta, \quad (17)$$

where  $\mathcal{B}$  denotes the set of all bonds,  $\Delta$  is a threshold,  $r^{ij}(T)$  is the bond length between atoms  $i$  and  $j$  at time  $T$ , and  $b^{ij}$  is the corresponding equilibrium bond length, computed as the average bond length using the reference DFT data. For the MD17 dataset, we adopted  $\Delta = 0.5 \text{ \AA}$  as in Ref. [43], and the MD simulations were performed at 500 K for 300 ps with a timestep of 0.5 fs, using the Nosé–Hoover thermostat.

## DATA AVAILABILITY

The new bilayer graphene dataset is provided at [https://github.com/wengroup/camp\\_run](https://github.com/wengroup/camp_run). The other datasets used in this work are publicly available; the LiPS dataset: <https://archive.materialscloud.org/record/2022.45>, the water dataset: <https://doi.org/10.1073/pnas.1815117116>, and the MD17 dataset: <http://www.sgdml.org>.

## CODE AVAILABILITY

The code for the CAMP model is available at <https://github.com/wengroup/camp>. Scripts for training models, running MD simulations, and analyzing the results are at [https://github.com/wengroup/camp\\_run](https://github.com/wengroup/camp_run).

## AUTHOR CONTRIBUTIONS

M.W.: project conceptualization, model development, data analysis, writing - original draft, writing - review, and supervision. W.F.H, J.D. and S.A.: data analysis and writing - review.

## CONFLICTS OF INTEREST

There are no conflicts of interest to declare.

## ACKNOWLEDGEMENTS

This work is supported by the National Science Foundation under Grant No. 2316667 and the startup funds from the Presidential Frontier Faculty Program at the University of Houston. This work was completed with computational resources provided by the Research Computing Data Core at the University of Houston.

## REFERENCES

- [1] B. Huang and O. A. von Lilienfeld, Ab initio machine learning in chemical compound space, *Chemical Reviews* **121**, 10001 (2021).
- [2] O. T. Unke, S. Chmiela, H. E. Sauceda, M. Gastegger, I. Poltavsky, K. T. Schütt, A. Tkatchenko, and K.-R. Müller, Machine learning force fields, *Chemical Reviews* **121**, 10142 (2021).
- [3] V. L. Deringer, A. P. Bartók, N. Bernstein, D. M. Wilkins, M. Ceriotti, and G. Csányi, Gaussian process regression for materials and molecules, *Chemical Reviews* **121**, 10073 (2021).
- [4] M. Wen, Y. Afshar, R. S. Elliott, and E. B. Tadmor, Kliff: A framework to develop physics-based and machine learning interatomic potentials, *Computer Physics Communications* **272**, 108218 (2022).
- [5] M. S. Daw and M. I. Baskes, Embedded-atom method: Derivation and application to impurities, surfaces, and other defects in metals, *Physical Review B* **29**, 6443 (1984).
- [6] J. Behler and M. Parrinello, Generalized neural-network representation of high-dimensional potential-energy surfaces, *Physical review letters* **98**, 146401 (2007).
- [7] A. P. Bartók, M. C. Payne, R. Kondor, and G. Csányi, Gaussian approximation potentials: The accuracy of quantum mechanics, without the electrons, *Physical review letters* **104**, 136403 (2010).
- [8] S. Chmiela, A. Tkatchenko, H. E. Sauceda, I. Poltavsky, K. T. Schütt, and K.-R. Müller, Machine learning of accurate energy-conserving molecular force fields, *Science Advances* **3**, e1603015 (2017).
- [9] L. Zhang, J. Han, H. Wang, R. Car, and W. E, Deep potential molecular dynamics: A scalable model with the accuracy of quantum mechanics, *Physical Review Letters* **120**, 143001 (2018).
- [10] K. T. Schütt, H. E. Sauceda, P.-J. Kindermans, A. Tkatchenko, and K.-R. Müller, Schnet – a deep learning architecture for molecules and materials, *Journal of Chemical Physics* **148**, 241722 (2018).
- [11] R. Zubatyuk, J. S. Smith, J. Leszczynski, and O. Isayev, Accurate and transferable multitask prediction of chemical properties with an atoms-in-molecules neural network, *Science Advances* **5**, eaav6490 (2019).
- [12] J. Gastegger, J. Groß, and S. Günnemann, Directional message passing for molecular graphs, in *International Conference on Learning Representations (ICLR)* (2020).
- [13] K. Schütt, O. Unke, and M. Gastegger, Equivariant message passing for the prediction of tensorial properties and molecular spectra, in *International Conference on Machine Learning*, Vol. 139 (PMLR, 2021) pp. 9377–9388.
- [14] T. W. Ko, J. A. Finkler, S. Goedecker, and J. Behler, A fourth-generation high-dimensional neural network potential with accurate electrostatics including non-local charge transfer, *Nature Communications* **12**, 398 (2021).
- [15] O. T. Unke, S. Chmiela, M. Gastegger, K. T. Schütt, H. E. Sauceda, and K.-R. Müller, SpookyNet: Learning force fields with electronic degrees of freedom and nonlocal effects, *Nature communications* **12**, 7273 (2021).
- [16] I. Batatia, D. P. Kovacs, G. Simm, C. Ortner, and G. Csányi, Mace: Higher order equivariant message passing neural networks for fast and accurate force fields, *Advances in Neural Information Processing Systems* **35**, 11423 (2022).
- [17] S. Batzner, A. Musaelian, L. Sun, M. Geiger, J. P. Mailoa, M. Kornbluth, N. Molinari, T. E. Smidt, and B. Kozinsky, E(3)-equivariant graph neural networks for data-efficient and accurate interatomic potentials, *Nature Communications* **13**, 1 (2022).
- [18] S. Takamoto, S. Izumi, and J. Li, Teanet: Universal neural network interatomic potential inspired by iterative electronic relaxations, *Computational Materials Science* **207**, 111280 (2022).
- [19] G. Simeon and G. De Fabritiis, TensorNet: cartesian tensor representations for efficient learning of molecular potentials, in *Guide Proceedings* (Curran Associates Inc., 2023) pp. 37334–37353.
- [20] M. Wen and E. B. Tadmor, Uncertainty quantification in molecular simulations with dropout neural network potentials, *npj Computational Materials* **6**, 124 (2020).
- [21] A. Zhu, S. Batzner, A. Musaelian, and B. Kozinsky, Fast uncertainty estimates in deep learning interatomic potentials, *Journal of Chemical Physics* **158**, 10.1063/5.0136574 (2023).
- [22] A. R. Tan, S. Urata, S. Goldman, J. C. B. Dietschreit, and R. Gómez-Bombarelli, Single-model uncertainty quantification in neural network potentials does not consistently outperform model ensembles, *npj Computational Materials* **9**, 1 (2023).
- [23] J. A. Vita, A. Samanta, F. Zhou, and V. Lordi, Ltau-ff: Loss trajectory analysis for uncertainty in atomistic force fields, *ArXiv e-prints* 10.48550/arXiv.2402.00853 (2024), 2402.00853.
- [24] J. Dai, S. Adhikari, and M. Wen, Uncertainty quantification and propagation in atomistic machine learning, *ArXiv e-prints* 10.48550/arXiv.2405.02461 (2024), 2405.02461.
- [25] J. Gilmer, S. S. Schoenholz, P. F. Riley, O. Vinyals, and G. E. Dahl, Neural message passing for quantum chemistry, in *International Conference on Machine Learning* (PMLR, 2017) pp. 1263–1272.
- [26] C. Chen and S. P. Ong, A universal graph deep learning interatomic potential for the periodic table, *Nature Computational Science* **2**, 718 (2022).
- [27] S. Takamoto, C. Shinagawa, D. Motoki, K. Nakago, W. Li, I. Kurata, T. Watanabe, Y. Yayama, H. Iriguchi, Y. Asano, T. Onodera, T. Ishii, T. Kudo, H. Ono, R. Sawada, R. Ishitani, M. Ong, T. Yamaguchi, T. Kataoka, A. Hayashi, N. Charoenphakdee, and T. Ibuka, Towards universal neural network potential for material discovery applicable to arbitrary combination of

- 45 elements, *Nature Communications* **13**, 1 (2022).
- [28] B. Deng, P. Zhong, K. Jun, J. Riebesell, K. Han, C. J. Bartel, and G. Ceder, Chgnet as a pretrained universal neural network potential for charge-informed atomistic modelling, *Nature Machine Intelligence* **5**, 1031 (2023).
- [29] I. Batatia, P. Benner, Y. Chiang, A. M. Elena, D. P. Kovács, J. Riebesell, X. R. Advincula, M. Asta, M. Avaylon, W. J. Baldwin, F. Berger, N. Bernstein, A. Bhowmik, S. M. Blau, V. Cărare, J. P. Darby, S. De, F. Della Pia, V. L. Deringer, R. Elijošius, Z. El-Machachi, F. Falcioni, E. Fako, A. C. Ferrari, A. Genreith-Schriever, J. George, R. E. A. Goodall, C. P. Grey, P. Grigorev, S. Han, W. Handley, H. H. Heenen, K. Hermansson, C. Holm, J. Jaafar, S. Hofmann, K. S. Jakob, H. Jung, V. Kapil, A. D. Kaplan, N. Karimitari, J. R. Kermode, N. Kroupa, J. Kullgren, M. C. Kuner, D. Kuryla, G. Liepuoniute, J. T. Margraf, I.-B. Magdău, A. Michaelides, J. H. Moore, A. A. Naik, S. P. Niblett, S. W. Norwood, N. O'Neill, C. Ortner, K. A. Persson, K. Reuter, A. S. Rosen, L. L. Schaaf, C. Schran, B. X. Shi, E. Sivonxay, T. K. Stenczel, V. Svahn, C. Sutton, T. D. Swinburne, J. Tilly, C. van der Oord, E. Varga-Umbrich, T. Vegge, M. Vondrák, Y. Wang, W. C. Witt, F. Zills, and G. Csányi, A foundation model for atomistic materials chemistry, *ArXiv e-prints* 10.48550/arXiv.2401.00096 (2023), 2401.00096.
- [30] F. Xie, T. Lu, S. Meng, and M. Liu, Gptff: A high-accuracy out-of-the-box universal ai force field for arbitrary inorganic materials, *Science Bulletin* **69**, 3525 (2024).
- [31] D. Zhang, X. Liu, X. Zhang, C. Zhang, C. Cai, H. Bi, Y. Du, X. Qin, A. Peng, J. Huang, B. Li, Y. Shan, J. Zeng, Y. Zhang, S. Liu, Y. Li, J. Chang, X. Wang, S. Zhou, J. Liu, X. Luo, Z. Wang, W. Jiang, J. Wu, Y. Yang, J. Yang, M. Yang, F.-Q. Gong, L. Zhang, M. Shi, F.-Z. Dai, D. M. York, S. Liu, T. Zhu, Z. Zhong, J. Lv, J. Cheng, W. Jia, M. Chen, G. Ke, W. E. L. Zhang, and H. Wang, Dpa-2: a large atomic model as a multi-task learner, *ArXiv e-prints* 10.48550/arXiv.2312.15492 (2023), 2312.15492.
- [32] H. Yang, C. Hu, Y. Zhou, X. Liu, Y. Shi, J. Li, G. Li, Z. Chen, S. Chen, C. Zeni, M. Horton, R. Pinsler, A. Fowler, D. Zügner, T. Xie, J. Smith, L. Sun, Q. Wang, L. Kong, C. Liu, H. Hao, and Z. Lu, Mattersim: A deep learning atomistic model across elements, temperatures and pressures, *ArXiv e-prints* 10.48550/arXiv.2405.04967 (2024), 2405.04967.
- [33] J. S. Smith, O. Isayev, and A. E. Roitberg, Ani-1: an extensible neural network potential with dft accuracy at force field computational cost, *Chemical Science* **8**, 3192 (2017).
- [34] A. P. Thompson, L. P. Swiler, C. R. Trott, S. M. Foiles, and G. J. Tucker, Spectral neighbor analysis method for automated generation of quantum-accurate interatomic potentials, *Journal of Computational Physics* **285**, 316 (2015).
- [35] R. Drautz, Atomic cluster expansion for accurate and transferable interatomic potentials, *Physical Review B* **99**, 014104 (2019).
- [36] A. V. Shapeev, Moment tensor potentials: A class of systematically improvable interatomic potentials, *Multiscale Modeling & Simulation* (2016).
- [37] G. Dusson, M. Bachmayr, G. Csányi, R. Drautz, S. Etter, C. van der Oord, and C. Ortner, Atomic cluster expansion: Completeness, efficiency and stability, *Journal of Computational Physics* **454**, 110946 (2022).
- [38] B. Cheng, Cartesian atomic cluster expansion for machine learning interatomic potentials, *npj Computational Materials* **10**, 1 (2024).
- [39] B. Cheng, E. A. Engel, J. Behler, C. Dellago, and M. Ceriotti, Ab initio thermodynamics of liquid and solid water, *Proceedings of the National Academy of Sciences* **116**, 1110 (2019).
- [40] M. Wen and E. B. Tadmor, Hybrid neural network potential for multilayer graphene, *Physical Review B* **100**, 195419 (2019).
- [41] I. S. Novikov, K. Gubaev, E. V. Podryabinkin, and A. V. Shapeev, The mlp package: moment tensor potentials with mpi and active learning, *Machine Learning: Science and Technology* **2**, 025002 (2020).
- [42] K. He, X. Zhang, S. Ren, and J. Sun, Deep residual learning for image recognition, *ArXiv e-prints* 10.48550/arXiv.1512.03385 (2015), 1512.03385.
- [43] X. Fu, Z. Wu, W. Wang, T. Xie, S. Ketten, R. Gomez-Bombarelli, and T. S. Jaakkola, Forces are not enough: Benchmark and critical evaluation for machine learning force fields with molecular simulations, *Transactions on Machine Learning Research* (2023).
- [44] L. Zhang, J. Han, H. Wang, W. Saidi, R. Car, and W. E, End-to-end symmetry preserving inter-atomic potential energy model for finite and extended systems, in *Advances in Neural Information Processing Systems*, Vol. 31, edited by S. Bengio, H. Wallach, H. Larochelle, K. Grauman, N. Cesa-Bianchi, and R. Garnett (Curran Associates, Inc., 2018).
- [45] Y. Liu, L. Wang, M. Liu, Y. Lin, X. Zhang, B. Oztekin, and S. Ji, Spherical message passing for 3d molecular graphs, in *International Conference on Learning Representations* (2022).
- [46] W. Hu, M. Shuaibi, A. Das, S. Goyal, A. Sriram, J. Leskovec, D. Parikh, and C. L. Zitnick, Forcenet: A graph neural network for large-scale quantum calculations, *ArXiv e-prints* 10.48550/arXiv.2103.01436 (2021), 2103.01436.
- [47] J. Gasteiger, F. Becker, and S. Günnemann, Gemnet: Universal directional graph neural networks for molecules, in *Advances in Neural Information Processing Systems*, Vol. 34, edited by M. Ranzato, A. Beygelzimer, Y. Dauphin, P. Liang, and J. W. Vaughan (Curran Associates, Inc., 2021) pp. 6790–6802.
- [48] A. Soper, F. Bruni, and M. Ricci, Site-site pair correlation functions of water from 25 to 400 c: Revised analysis of new and old diffraction data, *The Journal of chemical physics* **106**, 247 (1997).
- [49] L. B. Skinner, C. J. Benmore, J. C. Neufeind, and J. B. Parise, The structure of water around the compressibility minimum, *Journal of Chemical Physics* **141**, 10.1063/1.4902412 (2014).
- [50] Y. Zhang, J. Xia, and B. Jiang, Physically motivated recursively embedded atom neural networks: Incorporating local completeness and nonlocality, *Physical Review Letters* **127**, 156002 (2021).
- [51] O. Marsalek and T. E. Markland, Quantum dynamics and spectroscopy of ab initio liquid water: The interplay of nuclear and electronic quantum effects, *Journal of Physical Chemistry Letters* **8**, 1545 (2017).
- [52] J. Gasteiger, C. Yeshwanth, and S. Günnemann, Directional message passing on molecular graphs via synthetic

- coordinates, in *Advances in Neural Information Processing Systems*, Vol. 34, edited by M. Ranzato, A. Beygelzimer, Y. Dauphin, P. Liang, and J. W. Vaughan (Curran Associates, Inc., 2021) pp. 15421–15433.
- [53] M. Haghighatlari, J. Li, X. Guan, O. Zhang, A. Das, C. J. Stein, F. Heidar-Zadeh, M. Liu, M. Head-Gordon, L. Bertels, H. Hao, I. Leven, and T. Head-Gordon, Newtonnet: a newtonian message passing network for deep learning of interatomic potentials and forces, *Digital Discovery* **1**, 333 (2022).
- [54] S. J. Stuart, A. B. Tutein, and J. A. Harrison, A reactive potential for hydrocarbons with intermolecular interactions, *J. Chem. Phys.* **112**, 6472 (2000).
- [55] T. C. O'Connor, J. Andzelm, and M. O. Robbins, AIREBO-m: A reactive model for hydrocarbons at extreme pressures, *J. Chem. Phys.* **142**, 024903 (2015).
- [56] J. H. Los and A. Fasolino, Intrinsic long-range bond-order potential for carbon: Performance in monte carlo simulations of graphitization, *Phys. Rev. B* **68**, 024107 (2003).
- [57] J. E. Lennard-Jones, Cohesion, *Proceedings of the Physical Society* **43**, 461 (1931).
- [58] A. K. Geim and I. V. Grigorieva, Van der waals heterostructures, *Nature* **499**, 419 (2013).
- [59] M. Wen, S. Carr, S. Fang, E. Kaxiras, and E. B. Tadmor, Dihedral-angle-corrected registry-dependent interlayer potential for multilayer graphene structures, *Physical Review B* **98**, 235404 (2018).
- [60] J. P. Perdew, K. Burke, and M. Ernzerhof, Generalized gradient approximation made simple, *Physical Review Letters* **77**, 3865 (1996).
- [61] A. Tkatchenko, R. A. DiStasio, R. Car, and M. Scheffler, Accurate and efficient method for many-body van der waals interactions, *Physical Review Letters* **108**, 236402 (2012).
- [62] A. Paszke, S. Gross, F. Massa, A. Lerer, J. Bradbury, G. Chanan, T. Killeen, Z. Lin, N. Gimelshein, L. Antiga, A. Desmaison, A. Köpf, E. Yang, Z. DeVito, M. Raison, A. Tejani, S. Chilamkurthy, B. Steiner, L. Fang, J. Bai, and S. Chintala, Pytorch: An imperative style, high-performance deep learning library, *ArXiv e-prints* 10.48550/arXiv.1912.01703 (2019), 1912.01703.
- [63] pytorch-lightning (2024), [Online; accessed 2. Oct. 2024].
- [64] D. P. Kingma and J. Ba, Adam: A method for stochastic optimization, *ArXiv e-prints* 10.48550/arXiv.1412.6980 (2014), 1412.6980.
- [65] A. H. Larsen, J. J. Mortensen, J. Blomqvist, I. E. Castelli, R. Christensen, M. Dulak, J. Friis, M. N. Groves, B. Hammer, C. Hargus, E. D. Hermes, P. C. Jennings, P. B. Jensen, J. Kermode, J. R. Kitchin, E. L. Kolsbjerg, J. Kubal, K. Kaasbjerg, S. Lysgaard, J. B. Maronsson, T. Maxson, T. Olsen, L. Pastewka, A. Peterson, C. Rostgaard, J. Schiøtz, O. Schütt, M. Strange, K. S. Thygesen, T. Vegge, L. Vilhelmsen, M. Walter, Z. Zeng, and K. W. Jacobsen, The atomic simulation environment—a python library for working with atoms, *Journal of Physics: Condensed Matter* **29**, 273002 (2017).

**Supplementary Information for:**  
**Cartesian Atomic Moment Machine Learning**  
**Interatomic Potentials**

Mingjian Wen,<sup>\*</sup> Wei-Fan Huang, Jin Dai, and Santosh Adhikari

*Department of Chemical and Biomolecular Engineering,*

*University of Houston, Houston, TX, 77204, USA*

arXiv:2411.12096v1 [cond-mat.mtrl-sci] 18 Nov 2024

## 1. ATOMIC MOMENT TENSOR CONSTRUCTION EXAMPLE

Here, we give concrete examples of constructing the atomic moment tensors  $\mathbf{M}$  up to a rank of  $v_{\max} = 2$ . Higher-rank ones can be constructed similarly.

Let's start by considering the atomic moment in Eq. (5) in the main text. For ease of discussion, we copy the equation below:

$$\mathbf{M}_{uv,p}^i = \sum_{j \in \mathcal{N}_i} R_{uvv_1v_2} \mathbf{h}_{uv_1}^j \cdot (c) \cdot \mathbf{D}_{v_2}^{ij}. \quad (1)$$

The tensor ranks are only determined by the subscript  $v_1$ ,  $v_2$ , and  $v$ , and are not affected by either the radial function  $R$  or the summation over neighbors. Therefore, to simplify the presentation, we consider the below equation that captures the essence of Eq. (1):

$$\mathbf{M}_v = \mathbf{h}_{v_1} \cdot (c) \cdot \mathbf{D}_{v_2}, \quad (2)$$

where  $v_1$  denotes the rank of  $\mathbf{h}$  and  $v_2$  denotes the rank of  $\mathbf{D}$ ,  $v$  denotes the rank of  $\mathbf{M}$ , and  $\cdot(c)\cdot$  denotes the tensor contraction between the two tensors, with  $c$  being the contraction degree. If we choose to set the maximum allowed tensor rank to  $v_{\max} = 2$ , then we can have features up to rank 2 ( $\mathbf{h}_0$ ,  $\mathbf{h}_1$ , and  $\mathbf{h}_2$ ) and generalized dyadic tensors up to rank 2 as well ( $\mathbf{D}_0$ ,  $\mathbf{D}_1$ , and  $\mathbf{D}_2$ ).

The atomic moment tensor  $\mathbf{M}$  of different ranks are constructed by following two rules:

1. the rank of the feature tensor  $\mathbf{h}_{v_1}$  should be smaller than or equal to the rank of the dyadic tensor  $\mathbf{D}_{v_2}$ , i.e.,  $v_1 \leq v_2$ ; and
2. the indices of the feature tensor  $\mathbf{h}_{v_1}$  needs to be completely contracted away, i.e.,  $c = v_1$ .

These design principles ensure that information passes naturally from higher-rank tensors to lower-rank tensors, which is essential for modeling the potential energy surface, a scalar quantity. It also reduces the number of high-rank tensors, making the model more computationally efficient.

$\mathbf{M}_0$  tensors (scalars) are constructed from the below tensors:

$$\mathbf{h}_0 \cdot (0) \cdot \mathbf{D}_0 \quad (\text{product of two scalars})$$

---

\* mjwen@uh.edu



$\mathbf{h}_1 \cdot (1) \cdot \mathbf{D}_1$  (dot product of two vectors)

$\mathbf{h}_2 \cdot (2) \cdot \mathbf{D}_2$  (2-contraction between two second rank tensors, i.e.  $\sum_{ij} h^{ij} D^{ij}$ , where  $i$  and  $j$  are the tensor indices)

All three operations produce scalars. As mentioned in the main text, each of them is called a path and they are linearly combined to form the final atomic moment tensor  $\mathbf{M}_0$ .

Similarly,  $\mathbf{M}_1$  tensors (vectors) are constructed from the below tensors:

$\mathbf{h}_0 \cdot (0) \cdot \mathbf{D}_1$  (scalar multiplied by a vector)

$\mathbf{h}_1 \cdot (1) \cdot \mathbf{D}_2$  (1 contraction between a vector and a second rank tensor, i.e.,  $\sum_i h^i D^{ij}$ )

All four operations produce vectors and are linearly combined to form the final atomic moment tensor  $\mathbf{M}_1$ .

Finally,  $\mathbf{M}_2$  tensors (second rank tensors) are constructed from the below tensors:

$\mathbf{h}_0 \cdot (0) \cdot \mathbf{D}_2$  (scalar multiplied by a second rank tensor)

Both operations produce second-rank tensors and are linearly combined to form the final atomic moment tensor  $\mathbf{M}_2$ .

**We emphasize that, in all the above contractions, it does not matter which indices are used for contraction because both  $\mathbf{h}$  and  $\mathbf{D}$  are symmetric tensors. For example,  $\sum_i h^i D^{ij} = \sum_j h^j D^{ij}$ .**

## 2. HYPER MOMENT TENSOR CONSTRUCTION EXAMPLE

Here, we provide an example of constructing the hyper moment tensor  $\mathbf{H}$  up to a rank of  $v_{\max} = 3$ . We start with Eq. (7) in the main text (copied below for convenience):

$$\mathbf{H}_{uv,p} = \mathbf{M}_{uv_1} \cdot (c) \cdot \mathbf{M}_{uv_2} \cdot (c) \cdot \dots \cdot (c) \cdot \mathbf{M}_{uv_n}. \quad (3)$$

Similar to the atomic moment tensor construction, we consider the simplified version of Eq. (3):

$$\mathbf{H}_v = \mathbf{M}_{v_1} \cdot (c_1) \cdot \mathbf{M}_{v_2} \cdot (c_2) \cdot \dots \cdot (c_{n-1}) \cdot \mathbf{M}_{v_n} \quad (4)$$

where  $v_1, v_2, \dots, v_n$  denote the ranks of the atomic moment tensors  $\mathbf{M}$  and  $v$  denotes the rank of output the hyper moment. For a maximum allowed tensor rank of  $v_{\max} = 2$ , we can have atomic moment tensors up to rank 3 ( $\mathbf{M}_0, \mathbf{M}_1, \mathbf{M}_2$ , and  $\mathbf{M}_3$ ).

Similar to the atomic moment tensor construction, the hyper moment tensors  $\mathbf{H}$  of different ranks are constructed by following two rules:

1. All contractions are between a previous tensor  $M_{v_1}, \dots, M_{v_{n-1}}$  and the last tensor  $M_{v_n}$  in the sequence. This implies that the rank of the previous tensor should be smaller than or equal to the rank of the last tensor, i.e.,  $v_i \leq v_n$ , where  $i = 1, 2, \dots, n - 1$ .
2. The indices of the previous tensor  $M_{v_1}, \dots, M_{v_{n-1}}$  need to be completely contracted away, i.e.,  $c_i = v_i$ .

Again, as mentioned in the main text, the guiding principle for constructing the hyper moment tensor is to result in the information flow from higher-rank tensors to lower-rank tensors. This is driven by the fact that we are modeling the potential energy surface, which is a scalar quantity. An added benefit is that this can also reduce the number of high-rank tensors, which can be computationally expensive to compute and store.

The hyper moment tensor  $\mathbf{H}$  of different ranks are constructed as follows.

$\mathbf{H}_0$  tensors (scalars) are constructed from the below tensors:

$$\mathbf{M}_0 \quad (\text{body order } 2)$$

$$\mathbf{M}_1 \cdot (1) \cdot \mathbf{M}_1 \quad (\text{body order } 3)$$

$$\mathbf{M}_2 \cdot (2) \cdot \mathbf{M}_2 \quad (\text{body order } 3)$$

$$\mathbf{M}_3 \cdot (3) \cdot \mathbf{M}_3 \quad (\text{body order } 3)$$

$$\mathbf{M}_1 \cdot (1) \cdot \mathbf{M}_1 \cdot (1) \cdot \mathbf{M}_2 \quad (\text{body order } 4)$$

$$\mathbf{M}_1 \cdot (1) \cdot \mathbf{M}_2 \cdot (2) \cdot \mathbf{M}_3 \quad (\text{body order } 4)$$

$$\mathbf{M}_1 \cdot (1) \cdot \mathbf{M}_1 \cdot (1) \cdot \mathbf{M}_1 \cdot (1) \cdot \mathbf{M}_3 \quad (\text{body order } 5)$$

All seven operations produce scalars and are linearly combined to form the final hyper moment tensor  $\mathbf{H}_0$ . As mentioned in the main text, it is required that all contractions are between a previous tensor and the last tensor in the sequence. For example, in  $\mathbf{M}_1 \cdot (1) \cdot \mathbf{M}_2 \cdot (2) \cdot \mathbf{M}_3$ , the double contraction between  $\mathbf{M}_2$  and  $\mathbf{M}_3$  is carried out first, and then the resultant vector is single-contracted with  $\mathbf{M}_1$ , i.e.,  $\sum_{ijk} M^i M^{jk} M^{ijk}$ , where  $i, j$ , and  $k$  are the tensor indices. Again, the order of the indices being selected for contractions does not matter because all the tensors are symmetric, for example,  $\sum_{ijk} M^i M^{jk} M^{ijk} = \sum_{ijk} M^k M^{ij} M^{ijk}$ .

Any number of atomic moment tensors can be used to construct a hyper moment tensor. This choice enables quick body order expansion of the potential energy surface. For example, in the first layer, each atomic moment tensor  $\mathbf{M}$ , irrespective of its rank, only captures two-body interactions. This is because the atomic moment is constructed from the scalar features and the dyadic tensors  $\mathbf{D}$ , which, in turn, depends only on an atom  $i$  and its neighbor  $j$ , involving only two atoms. With the moment tensor  $\mathbf{H}_0$  constructed above from the atomic moment tensors  $\mathbf{M}$ , the interaction body orders can reach 5 with only a single layer. This is analogous to the B basis used in ACE and MACE.

$\mathbf{H}_1$  tensors (vectors) are constructed from the below tensors:

$$\mathbf{M}_1$$

$$\mathbf{M}_1 \cdot (1) \cdot \mathbf{M}_2$$

$$\mathbf{M}_2 \cdot (2) \cdot \mathbf{M}_3$$

$$\mathbf{M}_1 \cdot (1) \cdot \mathbf{M}_1 \cdot (1) \cdot \mathbf{M}_3$$

$\mathbf{H}_2$  tensors (second rank tensors) are constructed from the below tensors:

$$\mathbf{M}_2$$

$$\mathbf{M}_1 \cdot (1) \cdot \mathbf{M}_3$$

$\mathbf{H}_3$  tensors (third rank tensors) are constructed from the below tensors:

$$\mathbf{M}_3$$

### 3. COMPLEXITY ANALYSIS

The time complexity of the CAMP model is dominated by the construction of the atomic moment tensors and the hyper moment tensors. As detailed in the above two sections, the atomic moment tensors are created by contracting two tensors as in Eq. (2). For this contraction, we have  $v = v_1 + v_2 - 2c$ , where  $c$  is the contraction degree. The time complexity is  $O(3^{v_1+v_2-c})$ . In Section 1, we have discussed that CAMP has the constraint that  $c = v_1$ . Then the time complexity of the atomic moment tensor is  $O(3^{v_2})$ . Let the maximum rank of the tensors in CAMP be  $v_{\max}$ , then tensors up to rank  $v_{\max}$  can be used in the atomic moment tensor construction. So,  $v_2 \leq v_{\max}$ . **Therefore, the time complexity of the**

**atomic moment tensor construction is  $O(3^{v_{\max}})$ .** For example, when  $v_{\max} = 2$  as discussed in Section 1, the operations of  $O(3^2)$  complexity are those involving  $\mathbf{D}_2$ .

The hyper moment tensors are constructed by contracting multiple tensors as in Eq. (4). In Section 2, we have discussed that CAMP has the constraint that  $c_i = v_i$ , and every contraction is between a previous tensor and the last tensor in the sequence. Therefore, in terms of the time complexity analysis, Eq. (4) is equivalent to

$$\mathbf{H}_v = \mathbf{T}_{v'} \cdot (c) \cdot \mathbf{M}_{v_n}, \quad (5)$$

where  $\mathbf{T}_{v'}$  represents the sequence of tensors  $\mathbf{M}_{v_1}, \dots, \mathbf{M}_{v_{n-1}}$ ,  $v' = v_1 + \dots + v_{n-1}$ , and  $c = v'$ . The time complexity of this contraction is  $O(3^{v'+v_n-c}) = O(3^{v_n})$ . Given that the maximum rank of the tensors in CAMP is  $v_{\max}$ , we have  $v_n \leq v_{\max}$ . **Therefore, the time complexity of the hyper moment tensor construction is  $O(3^{v_{\max}})$ .** For example, when  $v_{\max} = 3$  as discussed in Section 2, the operations of  $O(3^3)$  complexity are those involving  $\mathbf{M}_3$  as the last tensor in Eq. (4).

#### 4. EXTRA RESULTS

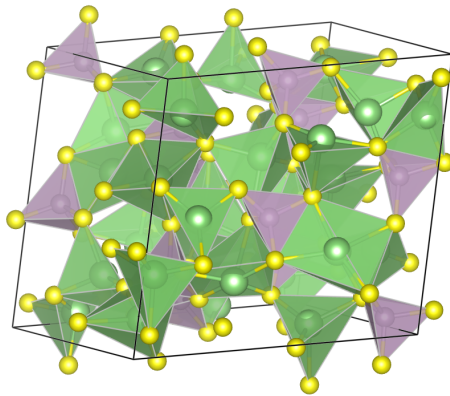


FIG. S1: Structure of the LiPS ( $\text{Li}_{6.75}\text{P}_3\text{S}_{11}$ ) crystal. The Li, P, and S atoms are shown in green, purple, and yellow, respectively. For the angular distribution function, the S-P-S angles in the purple tetrahedra are used.

TABLE S1: Running speed of various models (DeepPot-SE [1], SchNet [2], DimeNet [3], PaiNN [4], SphereNet [5], ForceNet [6], GemNet-T [7], GemNet-dT, NequIP [8]) for a water system with 192 atoms. The speed is measured as the number of frames per second (FPS) in an MD simulation using a single NVIDIA V100 GPU. All results, except for CACE [9] and CAMP, are obtained from water-1k results in Ref. [10]. Although these models are trained on a water dataset different from that used for CACE and CAMP, model running speed for water with 192 atoms are comparable.

| DeepPot-SE | SchNet | DimeNet | PaiNN | SphereNet | ForceNet | GemNet-T | GemNet-dT | NequIP | CACE | CAMP |
|------------|--------|---------|-------|-----------|----------|----------|-----------|--------|------|------|
| 61.8       | 99.2   | 16.4    | 54.5  | 3.0       | 68.1     | 15.4     | 34.5      | 3.9    | 9.8  | 14.2 |

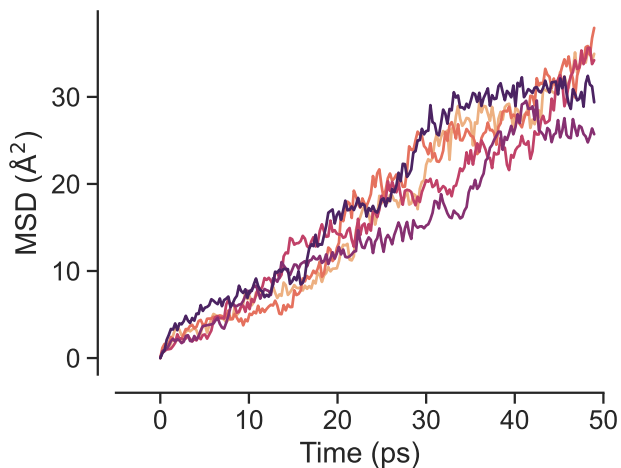


FIG. S2: MSD of LiPS using CAMP at a large timestep of 1 fs. The computed diffusivity is  $D = (1.11 \pm 0.11) \times 10^{-5} \text{ cm}^2/\text{s}$ .

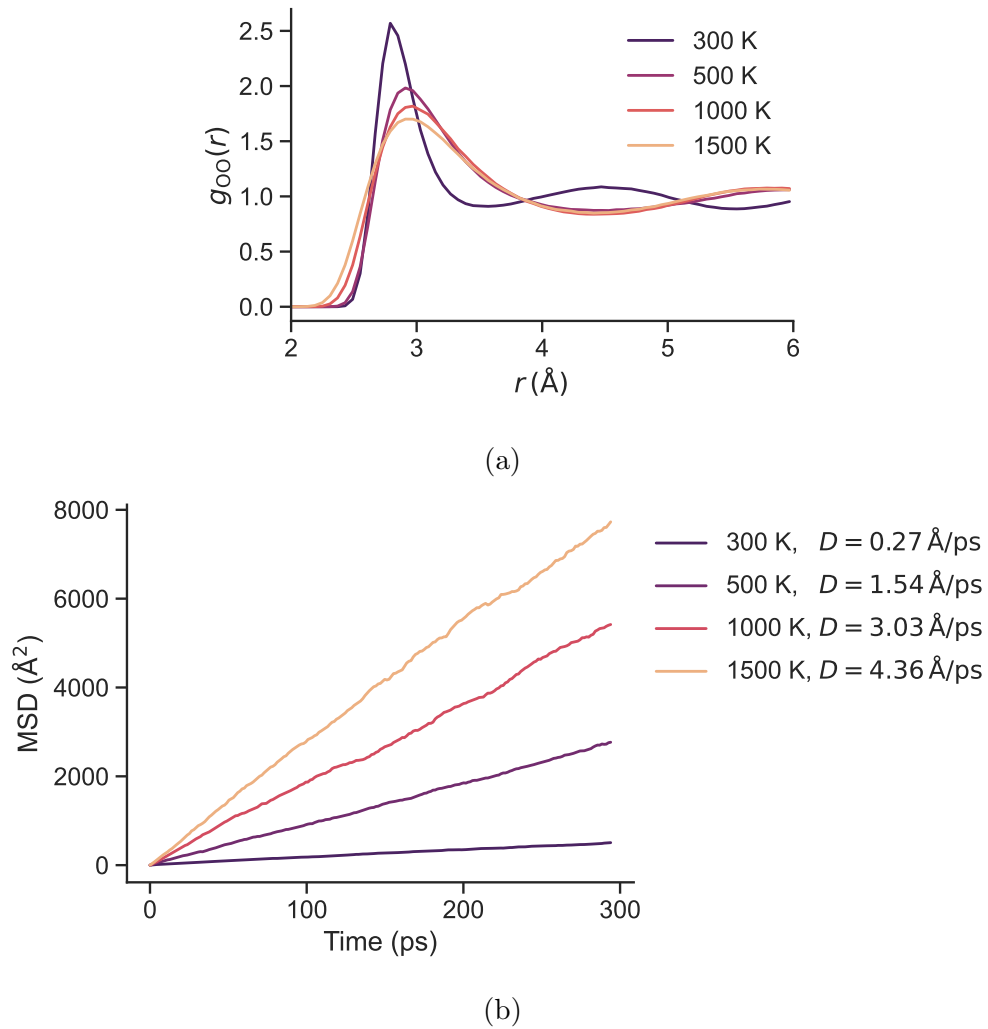


FIG. S3: MD simulation results of 512 water molecules using CAMP at various temperatures. (a) Radial distribution function. (b) Mean square displacement and the corresponding diffusion coefficient.

TABLE S2: Results of Aspirin and Ethanol trained on 9500 structures. Energy MAE in meV, force MAE in meV/Å, stability measured in picoseconds (larger the better). Results from all models (DeepPot-SE [1], SchNet [2], DimeNet [3], PaiNN [4], SphereNet [5], ForceNet [6], GemNet-T [7], and NequIP [8]) except for CAMP, are obtained from benchmarking study in Ref. [10].

| Molecule | Metric    | DeepPot-SE         | SchNet               | DimeNet            | PaiNN                | SphereNet           | ForceNet             | GemNet-T            | NequIP             | CAMP               |
|----------|-----------|--------------------|----------------------|--------------------|----------------------|---------------------|----------------------|---------------------|--------------------|--------------------|
| Aspirin  | Energy    |                    |                      |                    |                      |                     |                      |                     |                    | 5.0                |
|          | Forces    | 21.0               | 35.6                 | 10.0               | 9.2                  | 3.4                 | 22.1                 | 3.3                 | 2.3                | 5.5                |
|          | Stability | 9 <sub>(15)</sub>  | 26 <sub>(23)</sub>   | 54 <sub>(12)</sub> | 159 <sub>(121)</sub> | 141 <sub>(54)</sub> | 182 <sub>(144)</sub> | 72 <sub>(50)</sub>  | 300 <sub>(0)</sub> | 300 <sub>(0)</sub> |
|          | Speed     | 88.0               | 108.9                | 20.6               | 85.8                 | 17.5                | 137.3                | 28.2                | 8.4                | 35.0               |
| Ethanol  | Energy    |                    |                      |                    |                      |                     |                      |                     |                    | 2.1                |
|          | Force     | 8.9                | 16.8                 | 4.2                | 5.0                  | 1.7                 | 14.9                 | 2.1                 | 1.3                | 2.1                |
|          | Stability | 300 <sub>(0)</sub> | 247 <sub>(106)</sub> | 26 <sub>(10)</sub> | 86 <sub>(109)</sub>  | 33 <sub>(16)</sub>  | 300 <sub>(0)</sub>   | 169 <sub>(98)</sub> | 300 <sub>(0)</sub> | 300 <sub>(0)</sub> |
|          | Speed     | 101.0              | 112.6                | 21.4               | 87.3                 | 30.5                | 141.1                | 27.1                | 8.9                | 32.8               |

## 5. TRAINING DETAILS

TABLE S3: Training hyperparameters for the CAMP models.

| Dataset          | Allowed epochs | Early stopping patience | Batch size |
|------------------|----------------|-------------------------|------------|
| LiPS             | 5000           | 400                     | 2          |
| Water            | 10000          | 400                     | 4          |
| MD17             | 10000          | 800                     | 4          |
| Bilayer graphene | 1000           | 200                     | 4          |



TABLE S4: Optimal architectural hyperparameters for the CAMP models. The optimal hyperparameters are determined by a grid search:  $u \in [16, 32, 48, 64]$ ,  $v_{\max} \in [2, 3]$ ,  $T \in [1, 2, 3]$ , and  $r_{\text{cut}} \in [5, 5.5, 6]$ .

| Dataset          | Training set size | # channels | Max tensor rank | # layers | Cutoff                        |
|------------------|-------------------|------------|-----------------|----------|-------------------------------|
|                  |                   | $u$        | $v_{\max}$      | $T$      | $r_{\text{cut}} (\text{\AA})$ |
| LiPS             | 10                | 16         | 3               | 2        | 6                             |
| LiPS             | 100               | 16         | 3               | 2        | 6                             |
| LiPS             | 1000              | 48         | 3               | 3        | 6                             |
| LiPS             | 2500              | 64         | 3               | 3        | 6                             |
| LiPS             | 19000             | 48         | 3               | 3        | 6                             |
| Water            | 1433              | 32         | 2               | 3        | 5                             |
| Aspirin          | 950               | 48         | 3               | 2        | 6                             |
| Ethanol          | 950               | 48         | 3               | 2        | 6                             |
| Malonaldehyde    | 950               | 32         | 3               | 3        | 6                             |
| Naphthalene      | 950               | 32         | 3               | 3        | 6                             |
| Salicylic aci    | 950               | 48         | 3               | 2        | 5                             |
| Toluene          | 950               | 48         | 3               | 2        | 6                             |
| Uracil           | 950               | 48         | 3               | 3        | 5                             |
| Bilayer graphene | 5560              | 48         | 3               | 3        | 6                             |

## REFERENCES

- [1] L. Zhang, J. Han, H. Wang, W. Saidi, R. Car, and W. E, End-to-end symmetry preserving inter-atomic potential energy model for finite and extended systems, in *Advances in Neural Information Processing Systems*, Vol. 31, edited by S. Bengio, H. Wallach, H. Larochelle, K. Grauman, N. Cesa-Bianchi, and R. Garnett (Curran Associates, Inc., 2018).
- [2] K. T. Schütt, H. E. Sauceda, P.-J. Kindermans, A. Tkatchenko, and K.-R. Müller, Schnet – a deep learning architecture for molecules and materials, *Journal of Chemical Physics* **148**, 241722 (2018).
- [3] J. Gasteiger, J. Groß, and S. Günnemann, Directional message passing for molecular graphs,

- in *International Conference on Learning Representations (ICLR)* (2020).
- [4] K. Schütt, O. Unke, and M. Gastegger, Equivariant message passing for the prediction of tensorial properties and molecular spectra, in *Proceedings of the 38th International Conference on Machine Learning*, Proceedings of Machine Learning Research, Vol. 139, edited by M. Meila and T. Zhang (PMLR, 2021) pp. 9377–9388.
  - [5] Y. Liu, L. Wang, M. Liu, Y. Lin, X. Zhang, B. Oztekin, and S. Ji, Spherical message passing for 3d molecular graphs, in *International Conference on Learning Representations* (2022).
  - [6] W. Hu, M. Shuaibi, A. Das, S. Goyal, A. Sriram, J. Leskovec, D. Parikh, and C. L. Zitnick, Forcenet: A graph neural network for large-scale quantum calculations, ArXiv e-prints 10.48550/arXiv.2103.01436 (2021), 2103.01436.
  - [7] J. Gastegger, F. Becker, and S. Günnemann, Gemnet: Universal directional graph neural networks for molecules, in *Advances in Neural Information Processing Systems*, Vol. 34, edited by M. Ranzato, A. Beygelzimer, Y. Dauphin, P. Liang, and J. W. Vaughan (Curran Associates, Inc., 2021) pp. 6790–6802.
  - [8] S. Batzner, A. Musaelian, L. Sun, M. Geiger, J. P. Mailoa, M. Kornbluth, N. Molinari, T. E. Smidt, and B. Kozinsky, E(3)-equivariant graph neural networks for data-efficient and accurate interatomic potentials, *Nature Communications* **13**, 1 (2022).
  - [9] B. Cheng, Cartesian atomic cluster expansion for machine learning interatomic potentials, *npj Computational Materials* **10**, 1 (2024).
  - [10] X. Fu, Z. Wu, W. Wang, T. Xie, S. Keten, R. Gomez-Bombarelli, and T. S. Jaakkola, Forces are not enough: Benchmark and critical evaluation for machine learning force fields with molecular simulations, *Transactions on Machine Learning Research* (2023).